J. Fluid Mech. (2011), *vol.* 677, *pp.* 255–271.
doi:10.1017/jfm.2011.82

Flexibility effects on vortex formation of translating plates

DAEGYOUM KIM AND MORTEZA GHARIB†

Division of Engineering and Applied Science, California Institute of Technology, Pasadena, CA 91125, USA

(Received 9 February 2010; revised 27 January 2011; accepted 12 February 2011; first published online 18 April 2011)

Vortex structures made by impulsively translating low aspect-ratio plates are studied experimentally using defocusing digital particle image velocimetry. The investigation of translating plates with a 90° angle of attack is important since it is a fundamental model for a better understanding of drag-based propulsion systems. Rectangular flat-rigid, flexible and curved-rigid thin plates with the same aspect ratio are studied in order to develop qualitative and quantitative understanding of their vortex structures and hydrodynamic forces. We find that the vortex formation processes of all three cases are drastically different from each other. The interaction of leading-edge vortices and tip flow near the tip region is an important mechanism to distinguish vortex patterns among these three cases. The drag trends of three cases are correlated closely with vortex structure and circulation. The initial peak of hydrodynamic force in the flexible plate case is not as large as the initial peak of the flat and curved rigid plate cases during the acceleration phase. However, after the initial peak, the flexible plate generates a large force comparable to that of the flat-rigid plate case in spite of its deformed shape, which results from the slow development of the vortex structure.

Key words: propulsion, swimming/flying, vortex dynamics

1. Introduction

Flapping is a widely used locomotion mode of flying and swimming animals. Propulsion by flapping is used in both air and water in a broad range of Reynolds number regimes (Vogel 1996). Vortices created by flapping motion have been the central subject in studying animal locomotion since hydrodynamic forces and efficiency are closely related to the generation and transport of vortices. Researchers who have tried to identify vortices in animal locomotion using flow visualisation techniques have pointed to the possible correlation between aerodynamic or hydrodynamic force acting on flapping animals and observed vortices (e.g. Ellington *et al.* 1996; Drucker & Lauder 1999; Birch & Dickinson 2001; Srygley & Thomas 2002; Spedding, Rosen & Hedenstrom 2003). However, most of these experimental studies were based on two-dimensional flow field measurements which limited their ability to present a complete physical picture of these inherently three-dimensional unsteady flows.

The flow induced by the flapping motion of animals has some distinct features. The first feature is the small aspect ratio (AR) of the propulsors. Thus, the influence of tip

† Email address for correspondence: mgharib@caltech.edu

flow is significant. Second, the flow induced by the motion of a flapper is unsteady. Third, the angle of attack of the propulsor can be quite high. Finally, the propulsor is not rigid and has some flexibility in general. In this sense, impulsively starting flexible plates at a high angle of attack in low Reynolds number ranges will be an important model for an in-depth study relevant to animal locomotion. In particular, the study of passive deformation of flexible propulsors is a relevant topic for the design of bio-inspired propulsors since the flexibility feature is not common in these systems and the effect of flexibility on mechanical performance of such systems has not been well understood. Combes & Daniel (2003*a*, *b*) were among the first who measured the flexural stiffness of insect wings and found the anisotropy in the flexural stiffness in spanwise and chordwise directions. Combes & Daniel (2003*c*) proposed that passive wing deformation of their models was mainly caused by inertial–elastic force in rapid acceleration and deceleration, rather than aerodynamic force. From two-dimensional quantitative flow visualisation studies, Mountcastle & Daniel (2009) and Young *et al.* (2009) showed that the flexible wings of insects can be more efficient in lift generation than stiff wings.

Many studies have been performed for two-dimensional flow around a translating plate with a high angle of attack as a fundamental study for insect flight (e.g. Dickinson & Götz 1993; Pullin & Wang 2004; Wang 2004). Dickinson & Götz (1993) used impulsively translating plate models with various angles of attacks in the Reynolds number range of 10–1000. They showed that impulsively starting models and the resultant unsteady vortex generation process are important in the study of insect flights since the wings typically move a few chord lengths for each half-stroke. On the other hand, Ringuette, Milano & Gharib (2007) reported that, for plate models normal to the translating direction, the unsteady drag coefficient of the plate with small AR is bigger than the plate with large AR. They attributed their observations to the tip edge effect. Ringuette *et al.* (2007) obtained two-dimensional vorticity fields and calculated circulation at three sections using planar digital particle image velocimetry (DPIV). Because of the inherent limitation of planar DPIV, they could not obtain three-dimensional velocity and vorticity fields.

The main goal of our study is to understand the three-dimensional vortex formation process of low aspect-ratio plates whose surface is normal to the translating direction. We also study the effect of passive deformation of the plate on flow structure and force generation. For this purpose, we chose a relatively simple translating motion of rectangular plates of low AR, even though the flapping motions of the animal propulsors are very complex, and they have diverse shapes. By focusing on the translating motion of rectangular plates, we could isolate the effect of flexibility on flow structure from other effects, such as rotation and specific geometry. Using a water tank, flat-rigid and flexible polycarbonate plates of AR 3.75 with different flexural stiffnesses were translated impulsively with a 90° angle of attack. Only the spanwise bending of the flexible plate was considered in this study. A curved rigid plate, which has a similar shape to the flexible plate at its maximum deformation, was also chosen for comparison with the other cases. In order to map three-dimensional flow fields present in this study, we implemented defocusing digital particle image velocimetry (DDPIV, Willert & Gharib 1992; Pereira & Gharib 2002; Pereira *et al.* 2006).

2. Experimental setup

Figure 1(*a*) shows the experimental setup. A water tank with $870 \times 430 \times 360\,\mathrm{mm}^3$ dimensions was used for the experiment. Three polycarbonate plates ($\rho_m = 1.2\,\mathrm{g\,cm}^{-3}$)

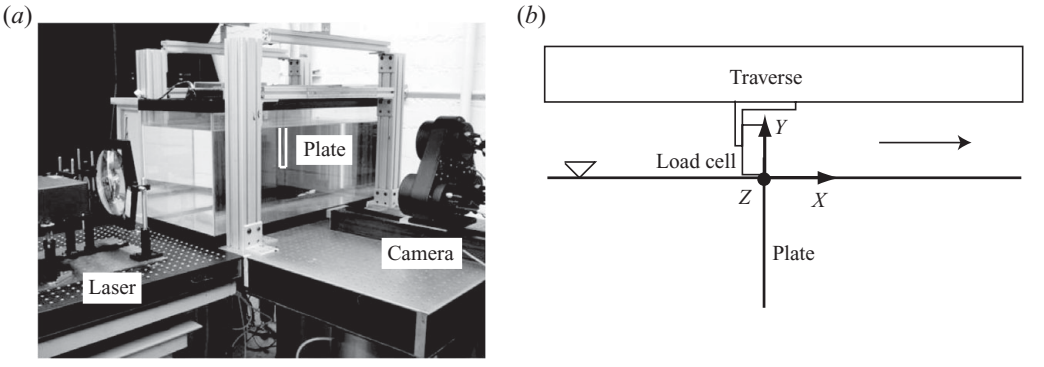

FIGURE 1. (*a*) Experimental setup. White lines are the edges of the plate model. (*b*) Details of the mechanical model from the camera view. The arrow indicates the moving direction of a traverse.

were used to represent *flat-rigid*, *flexible* and *curved-rigid* plates. The thickness h and Young's modulus E of the rigid plates were 1.52 mm and 2.3 GPa for the rigid plates and 0.25 mm and 2.4 GPa for the flexible plate. The Poisson ratio $\hat{\nu}$ of the plates was 0.37. Even though the plates with 1.52 mm thickness were not completely rigid, its deformation during translation was negligible and, thus, the *rigid* term is used as a counterpart to the *flexible* term. The plate was immersed vertically in the middle of the tank (figure 1*b*). The span length s immersed in the water was 150 mm, and the width of the plate c was 40 mm. Part of the plate above a free surface was attached firmly to a load cell (miniature beam type, Interface Inc.). A traverse with a lead-screw (Velmex Inc.) to translate the plate was driven by a stepper motor. The traverse accelerated for 0.25 s at the start and translated with a constant velocity U_c of 50 mm s^{-1}. The Reynolds number based on the constant traverse velocity and plate width ($Re = U_c c/\nu$) was 2000. During model translation, there was slight deformation of the free surface because of a low pressure region inside the vortex core on the free surface. However, the deformation of the free surface was less than a millimetre and negligible compared to the length scale of the model. If we assume the free surface is flat and the slip boundary condition is applicable on the free surface, the flow field and the model can be mirrored across the free surface. In other words, our model can be considered as a half of a twice longer model fully immersed in fluid. To make the curved shape for the curved-rigid plate, a hole near a tip edge was penetrated, and a thread was used to connect the hole and the load cell while keeping the plate curved. We tried to make the curved-rigid plate bend at the same degree as the flexible plate at its maximum deformation by comparing camera images of the curved-rigid and deformed flexible plates. However, there were some deviations in curvatures because it was difficult to match the shapes exactly. The origin of the coordinate system used in this study is on the free surface and between the two parallel vertical edges of the plate at the starting position. The x-axis is in the direction of plate translation, the y-axis is in the vertical direction and the z-axis is towards the camera (figure 1*b*). The flow field is symmetrical with respect to the $z = 0$ plane.

The DDPIV camera was placed in front of the water tank (figure 1*a*). The distance between the water tank and the camera was adjusted to position the camera probe volume in the middle of the tank. The tank was seeded with silver-coated ceramic spheres of mean diameter 100 μm (Conduct-o-fil, Potters Industries Inc.). An Nd:YAG laser (200 mJ pulse^{-1}, Gemini PIV, New Wave Research Inc.) was placed to the left

side of the camera and optical lenses were used to make a laser cone, which covered the camera probe volume. The traverse system, including the plate model and the load cell, was placed over the tank so that the plate model could be seen from the camera. A computer sent a trigger signal to synchronise the DDPIV camera frames, the laser pulses, and the motor operation. Image pairs were captured at a rate of 5 pairs s^{-1}. The time gap between two laser pulses to take a pair of images was 50 ms.

The images taken from the camera were processed with the in-house DDPIV software v4.6, based on Pereira & Gharib (2002) and Pereira *et al.* (2006). First, the three-dimensional coordinates of particles inside the tank were found. Then, from this information, velocity vectors of particles were calculated using a relaxation method of three-dimensional particle tracking (Pereira *et al.* 2006). The velocity vectors obtained from tracking particles are randomly spaced. The flow field with $160 \times 160 \times 140\,\text{mm}^3$ volume was cropped during these procedures. We decided to use cubic grids of size $3 \times 3 \times 3\,\text{mm}^3$ for the flow field. However, the number of cubic grids in the mapped domain was much larger than the number of randomly spaced velocity vectors obtained from one case ($\sim$5000). To increase the density of randomly spaced velocity vectors in a fluid domain, the experiment was repeated 20 times under the same conditions with an interval of 90 s. This interval was enough to settle the flow generated by the previous run. For each time step, the randomly spaced velocity vectors obtained from 20 cases were collected. Then, the collected velocity vectors were interpolated into cubic grids to produce a velocity field. After removing outlier vectors and applying a smoothing operator to velocity vectors, the vorticity field was obtained by a central difference scheme. For smooth rendering of three-dimensional iso-surfaces of vorticity magnitude, vorticity data were also smoothed. Because of the plate translation, it was necessary to map the longer flow volume along the x-axis. The initial position of the plate was moved back 80 mm for the second set of the experiment so that the plate showed up in the camera volume later. Then, the experiment was conducted again for the later stage of the plate motion. In order to track the shape of the flexible plate during translation, some seeding particles were attached to the edges of the plate with glue, and the plate was immersed in clean water. Through the DDPIV process, the deformed shape of the flexible plate could be obtained from the coordinate information of the seeding particles attached to the edges.

We also measured hydrodynamic drag forces acting on the plates with a load cell. The drag is the force acting on the plate in the negative x-direction. Force transducer outputs were amplified and low-pass filtered through a signal conditioner (SGA, Interface Inc.) and Matlab (The Mathworks Inc.) with 3 Hz cutoff frequency. Forces were also measured for the models in air in order to make sure that the inertial force experienced by the plate was negligible. The flexible plates showed that no measurable deformation occurred in this air experiment. These observations convinced us that our plates were deformed mainly due to hydrodynamic forces acting on them. Two definitions of drag coefficient were used in this paper. For the first drag coefficient definition C_D, the measured drag was non-dimensionalised by the immersed area of the plate $S(=sc,\ 150\,\text{mm} \times 40\,\text{mm})$ and the constant velocity of the traverse U_c (50 mm). For the second drag coefficient definition C_D^*, the measured drag was non-dimensionalised by the instantaneous frontal area of the plate that was projected on the yz-plane and the instantaneous forward velocity u_x of the plate,

$$C_D = \frac{D}{\frac{1}{2}\rho_f U_c^2 S}, \tag{2.1a}$$

$$C_D^* = \frac{D}{\frac{1}{2}\rho_f c \int_0^s u_x^2 \cos\theta(a)\,\mathrm{d}a}, \tag{2.1b}$$

where a is the curvilinear coordinate along the span from the base towards the tip, and $\theta(a)$ is the angle between the plate and the vertical y-axis.

Following Gharib, Rambod & Shariff (1998), a non-dimensional time T known as *formation time* was defined as $\int_0^{t_d} U(\tau)\,\mathrm{d}\tau/c$, where U is the traverse velocity, c is the plate width and t_d is the dimensional time. In figures of § 3, coordinate, velocity, vorticity, circulation and circulation rate are also non-dimensionalised,

$$\boldsymbol{x} = \frac{\boldsymbol{x}_d}{c}, \quad \boldsymbol{u} = \frac{\boldsymbol{u}_d}{U_c}, \quad \boldsymbol{\omega} = \frac{\boldsymbol{\omega}_d c}{U_c}, \quad \Gamma = \frac{\Gamma_d}{U_c c}, \quad \dot{\Gamma} = \frac{\dot{\Gamma}_d}{U_c^2}, \tag{2.2}$$

where the subscript d means the dimensional variable.

Two non-dimensional parameters are necessary to characterise the problem for the dynamical interaction of the deformable plate model and the surrounding fluid. Namely,

$$\frac{\rho_m h}{\rho_f c} = 0.046(\text{rigid})\,,\ 0.008(\text{flexible}), \quad \frac{EI}{\rho_f U_c^2 s^3} = 79.8(\text{rigid})\,,\ 0.4(\text{flexible}), \tag{2.3}$$

where EI is the flexural stiffness of plates per unit width, ρ_m and ρ_f are the density of plates and water and s, c and h are the span, the chord and the thickness of the plate inside the tank. Dynamically, the former parameter implies the relative magnitude of the inertial force at a spanwise plate section over the acceleration-reaction force of the surrounding fluid at the section. The latter indicates the ratio of the bending shear force of the plate to the inertial force of the fluid. In this study, the spanwise length s (150 mm) of the plate is relatively larger than the width c (40 mm); likewise, spanwise deformation is dominant over chordwise deformation. Therefore, we assume one-dimensional deformation of a beam type where the Poisson ratio does not affect the flexural stiffness $EI(= Eh^3/12)$.

3. Results and discussion

Figure 2(a) shows the plate shapes for the three cases considered in this study. The frontal area S_x of the curved-rigid plate is 0.9 of the flat-rigid plate frontal area, and the tip is positioned 62 mm behind from the base in the x-direction. For the flexible plate case, the deformation is shown at several formation times T. The flexible plate deforms maximally at $T = 2.1$. Afterwards, its deformation is relaxed, and the tip retracts back towards the original position. The change in the plate shape is negligible after $T = 5.3$. The x-directional velocity of the flexible plate at the four positions is plotted in figure 2(b). Obviously, the flexible plate has different forward velocities along the span. The flexible plate accelerates until about $T = 3.6$. The tip reaches its maximum forward velocity $u_x(= 1.3)$ at $T = 3.6$. In the following sections, we will refer to figure 2 to report our results.

3.1. *Formation of vortex structure*

Throughout this study, the vortices generated along two vertical long edges of the plate are termed leading-edge vortices (LEV) and the vortex along the horizontal short edge is termed as a tip vortex (TV). Iso-surfaces of vorticity magnitude are plotted in figure 3 for the flat-rigid plate case, figure 4 for the flexible plate case and figure 5

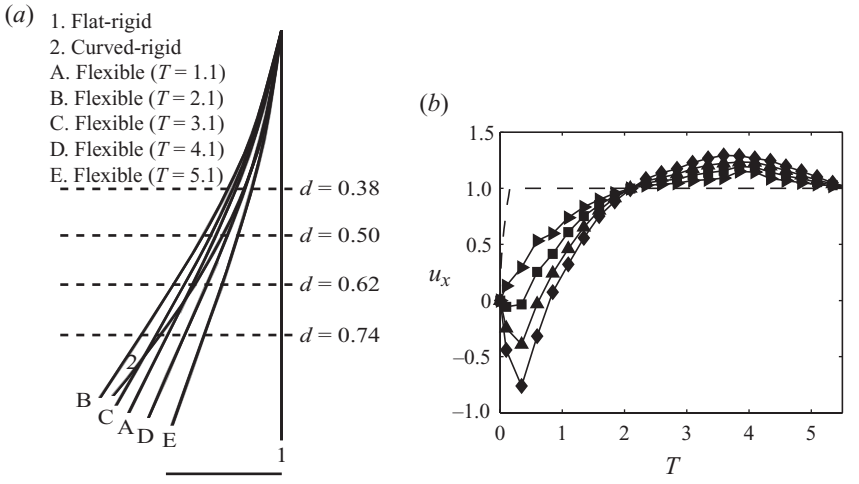

FIGURE 2. (*a*) Shapes of the plates during translation. In order to compare x-directional deviation of the tip from a vertical line, the plates are rearranged to have the same base position on the free surface. Four horizontal dashed lines are the sections where the strength and position of the vortex are evaluated. d is the normalised distance of the y-cross-sections from the free surface (vertical distance from the free surface/span length of the plate). A horizontal continuous line at the bottom is the distance which the traverse travels for $\Delta T = 1$. (*b*) Non-dimensional forward velocity u_x of the flexible plate at four positions along the span. The distance of the four positions from the base (free surface) along the span is 150 mm (tip, ◆), 125 mm (▲), 100 mm (■) and 75 mm (►), respectively. The dashed line is the velocity of the traverse.

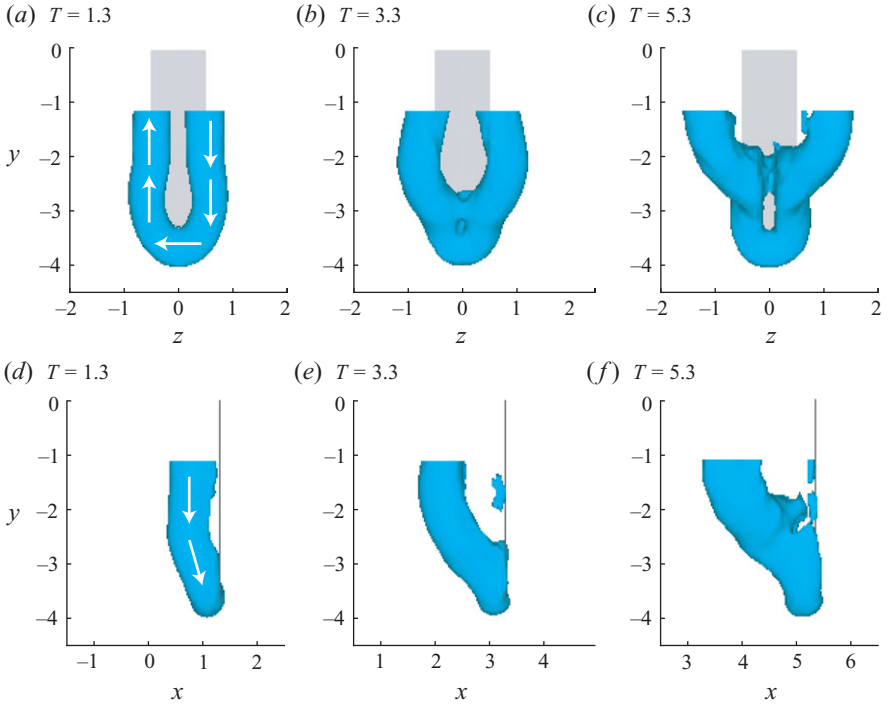

FIGURE 3. (Colour online available at journals.cambridge.org/FLM) Vortex formation process in the flat-rigid plate case (iso-surface of vorticity magnitude, $|\boldsymbol{\omega}| = 3.0$). (*a*)–(*c*) are from back view and (*d*)–(*f*) are from side view. White arrows in (*a*) and (*d*) show the rotating direction of the vortex by the right-hand rule.

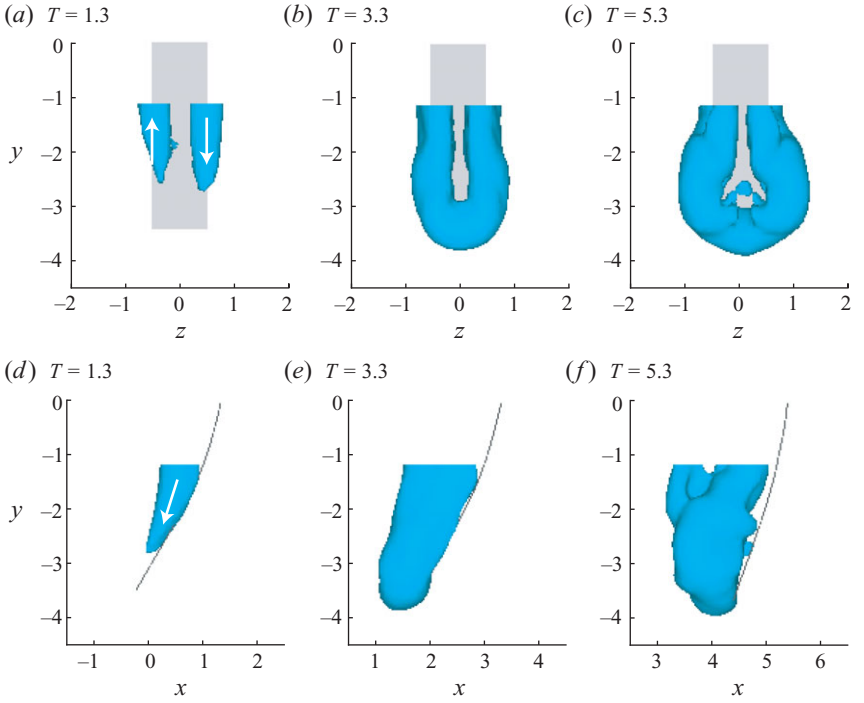

FIGURE 4. (Colour online) Vortex formation process in the flexible plate case (iso-surface of vorticity magnitude, $|\boldsymbol{\omega}| = 3.0$). (*a*)–(*c*) are from back view and (*d*)–(*f*) are from side view. White arrows in (*a*) and (*d*) show the rotating direction of the vortex by the right-hand rule.

for the curved-rigid plate case. The vorticity magnitude of $|\boldsymbol{\omega}| = 3.0$ was chosen to show the vortex core clearly. The plates shown in these figures are all immersed in water. The top 30 % of the plate was beyond the camera probe volume and, thus, the flow field near the top of the plate is absent. In order to quantify the position of the vortex, the centre of the LEV on the upper $d = 0.38$ and lower $d = 0.74$ planes of figure 2(*a*) was defined as $\int_{A_y} z\omega_y \, \mathrm{d}A / \int_{A_y} \omega_y \, \mathrm{d}A$, where A_y is the total fluid area of a y-section in the positive z side (figure 6). Because of the symmetry condition, only positive z side was considered. Similarly, the centre of the TV on the $z = 0$ plane was calculated from $\int_{A_z} y\omega_z \, \mathrm{d}A / \int_{A_z} \omega_z \, \mathrm{d}A$, where A_z is the total fluid area of the $z = 0$ plane. To avoid including noise, ω_y and ω_z whose magnitude are smaller than $0.5\,\mathrm{s}^{-1}$ were discarded in evaluating the vortex position.

In the flat-rigid plate case, a vortex sheet emanates from plate edges and rolls up along the edges when the plate starts. Near $T = 1.3$, the LEV in the mid-section of each side starts to get away from the plate and forms a curved shape. Whereas the LEV near the tip remains attached to the plate, the LEV in the upper part detaches from the plate and moves outwards in the z-direction. The z-position of the LEV centre at the $d = 0.38$ changes from $z = 0.44$ to 0.97 during $T = 1.3$–5.3 (figure 6*a*). At the same time, the LEV of the upper part slants onto the xz-plane, and the x-directional forward motion of the LEV in the upper part is delayed. Meanwhile, some part of the TV moves upwards in the positive y-direction continuously due to the tip flow (figures 3*c* and 3*f*). Between $T = 1.3$ and 5.3, the centre of the chordwise vorticity ω_z at the $z = 0$ plane moves from $y = -3.42$ to -2.86 (figure 6*b*). A similar behaviour has been reported by Ringuette *et al.* (2007). The upward motion of some

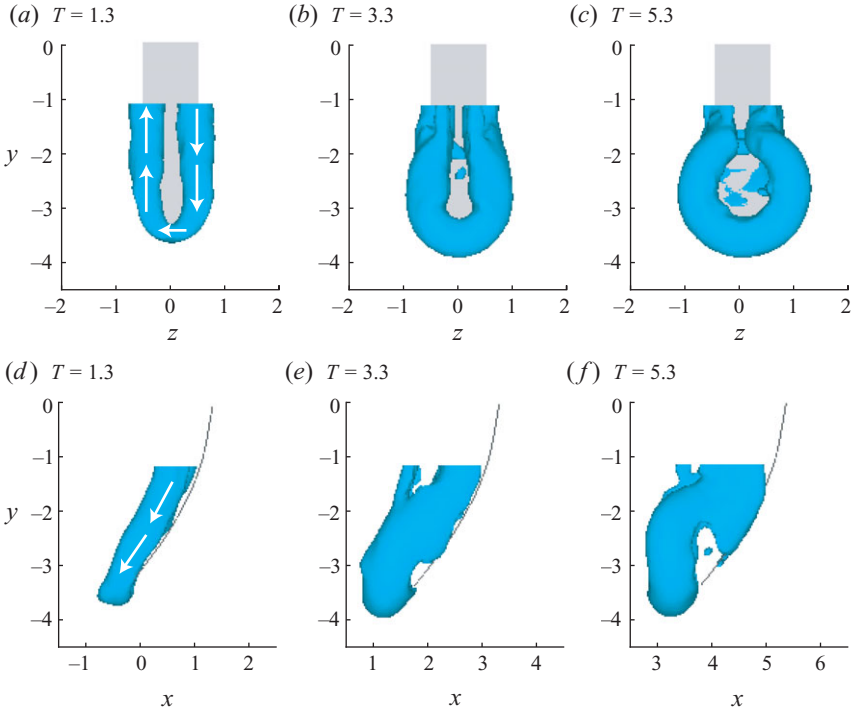

FIGURE 5. (Colour online) Vortex formation process in the curved-rigid plate case (iso-surface of vorticity magnitude, $|\boldsymbol{\omega}| = 3.0$). (*a*)–(*c*) are from back view and (*d*)–(*f*) are from side view. White arrows in (*a*) and (*d*) show the rotating direction of the vortex by the right-hand rule.

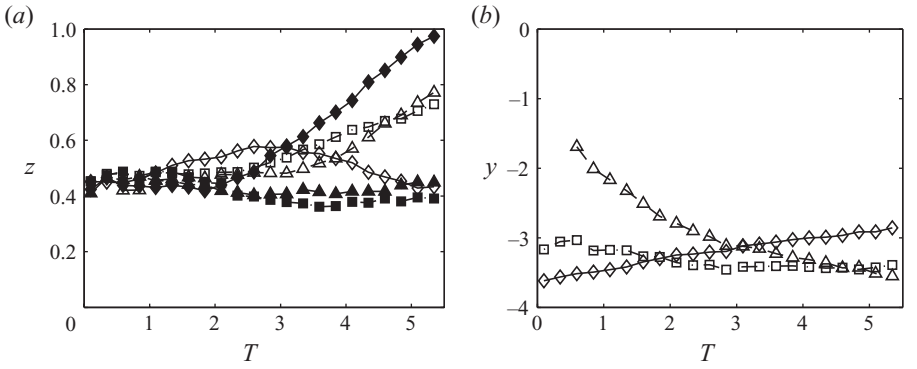

FIGURE 6. (*a*) *Z*-directional position of the LEV centre on the upper $d = 0.38$ and lower $d = 0.74$ sections of figure 2(*a*). (*b*) *Y*-directional position of the TV centre on the $z = 0$ plane. The position was non-dimensionalised by the chord *c*. In (*a*), for the flat-rigid plate, $d = 0.38$ (◆) and $d = 0.74$ (◇); for the flexible plate, $d = 0.38$ (▲) and $d = 0.74$ (△); for the curved-rigid plate, $d = 0.38$ (■) and $d = 0.74$ (□). In (*b*), the flat-rigid plate (◇), the flexible plate (△), and the curved-rigid plate (□). For the flexible plate case, first some points were not included in (*b*) because most of ω_z exists near the top of the plate beyond the mapped flow volume.

portion of the TV is concurrent with the tilting of the LEV onto the xz-plane during the full observation time of the experiment.

In the flexible plate case, the forward motion of the lower part of the plate is delayed due to bending of the plate at start (figure 2). Thus, the strong vortex

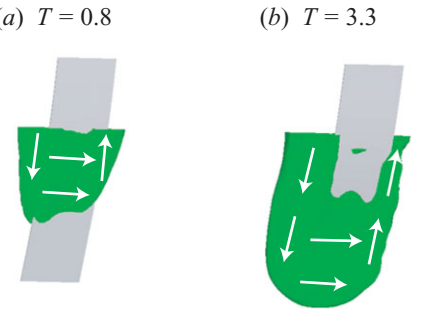

FIGURE 7. (Colour online) Vorticity distribution in front of the plate in the flexible plate case (iso-surface of vorticity magnitude, $|\boldsymbol{\omega}| = 1.6$). White arrows in (*a*) and (*b*) show the rotating direction of the LEVs and the boundary layer on the front surface of the plate. Between (*a*) and (*b*), the vortex sheet of negative ω_z starts to develop in the lower part of the front surface.

structure develops first in the upper part (figures 4*a* and 4*d*). As the lower part of the plate starts to move in the positive x-direction, the LEV and the TV begin to develop in the lower part as well. At the same time, the vortex sheet on the front surface of the plate, which connects two LEVs, strengthens in the lower part of the plate (figure 7). The vortex morphology follows the shape of the plate without exhibiting any distinct deformation until $T = 3.3$. However, after this time, the vortex deforms into a horseshoe shape in the lower region of the plate. During this deformation process of the lower LEV part, the vortex core in the upper part continues to elongate in the x-direction. Note that, in the flat-rigid plate case, the LEV in the upper part of the plate moves away from the plate early and maintains the circular vortex core. However, in the flexible plate case, the LEV in the upper part does not move outwards in the z-direction from the plate edge and ends up having an elongated vortex core. While the LEVs of the lower region move outwards in the z-direction, the LEVs in the upper region tend to move towards the symmetrical $z = 0$ plane, which results in a horseshoe-shaped vortex (figures 4*c* and 4*f*). However, the LEV's inward movement to the $z = 0$ plane is blocked by the LEV on the other side due to the imposed symmetric condition on the $z = 0$ plane. For this reason, the LEVs in the upper part elongate in the x-direction. While the LEV centre at the lower y-section ($d = 0.74$) moves from $z = 0.46$ to 0.77 during $T = 1.3$–5.3, the LEV centre at the upper y-section ($d = 0.38$) does not change noticeably in the z-direction, but stays near $z = 0.40$–0.45 during that time span (figure 6*a*).

For the curved-rigid plate case, the vortex in the lower part of the plate grows faster than that of the flexible plate case. The formation of the vortex into a horseshoe shape in the lower region is more distinct than that of the flexible plate case. The vortex system in the lower part of the plate becomes nearly a circular vortex (figure 5*c*). The severe elongation of the LEV core in the upper part of the plate is also found in this case. In the deformation process of the vortex, the LEV near the tip is tilted vertically (figure 5*f*).

3.2. *Effect of tip flow on vortex formation*

The outward motion of the upper LEV as shown in the flat-rigid plate and the severe elongation of the upper LEV core along the x-direction as shown in the flexible and curved-rigid plates are not present in the flow field of impulsively moving two-dimensional flat plates (Koumoutsakos & Shiels 1996). Thus, it is reasonable to conjecture that three-dimensional effects make the vortex formation process in our

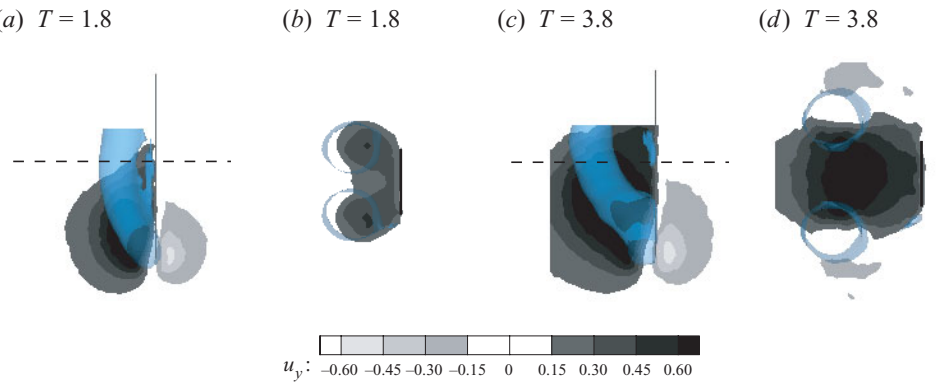

FIGURE 8. (Colour online) Y-directional flow distribution at $T = 1.8$ and 3.8 for the flat-rigid plate. The u_y contour of (a) and (c) is on the symmetrical $z = 0$ section (side view). The u_y contour of (b) and (d) is on the $d = 0.5$ section (top view). The dashed line in (a) and (c) is the position of the $d = 0.5$ section. The three-dimensional transparent surface is the iso-surface of vorticity magnitude ($|\boldsymbol{\omega}| = 3.0$).

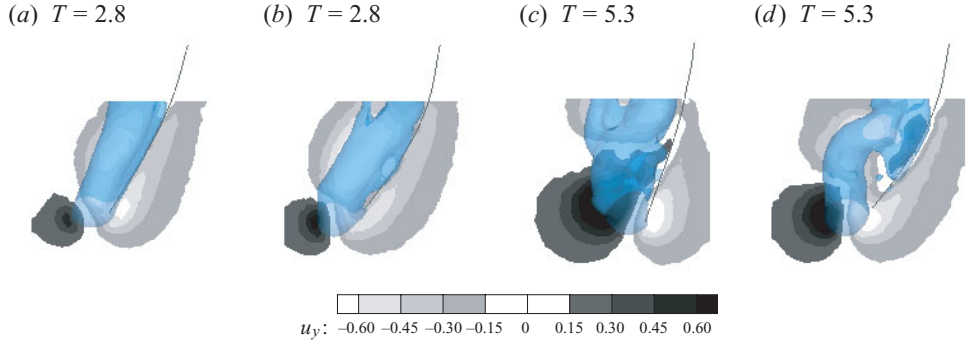

FIGURE 9. (Colour online) Y-directional flow distribution at $T = 2.8$ and 5.3 for the flexible plate ((a) and (c)) and the curved-rigid plate ((b) and (d)). The u_y contour is on the symmetrical $z = 0$ section (side view). The three-dimensional transparent surface is the iso-surface of vorticity magnitude ($|\boldsymbol{\omega}| = 3.0$).

cases drastically different from that of the two-dimensional model. It will be shown that the main three-dimensional factor for the observed differences among the three cases is the presence of upward flow (tip flow in the positive y-direction) near the tip region and its influence on the nearby vortex structure.

First, let us consider the flat-rigid plate case. When the plate starts to translate, upward flow is induced from the tip because forward motion of the plate creates a suction region behind the plate. The growing vortical flow of the tip moves up towards the inner region of the plate's backside. This upward flow near the tip interferes with the LEV formation process by being entrained to the upper part of the LEV. The entrainment of the tip flow enforces the LEV to move away from the plate's edge (figure 8). Once the LEV starts to move away from the plate, the upward flow becomes more dominant behind the plate. At the same time, some TV separates from the tip edge and shifts further up. This observation indicates that upward flow from the tip and its interaction with the LEV has a significant role in early deformation and outward motion of the LEV. In figure 8(d), the high magnitude of y-component of the velocity u_y is observed near the $z = 0$ plane between the plate and the LEVs. In other

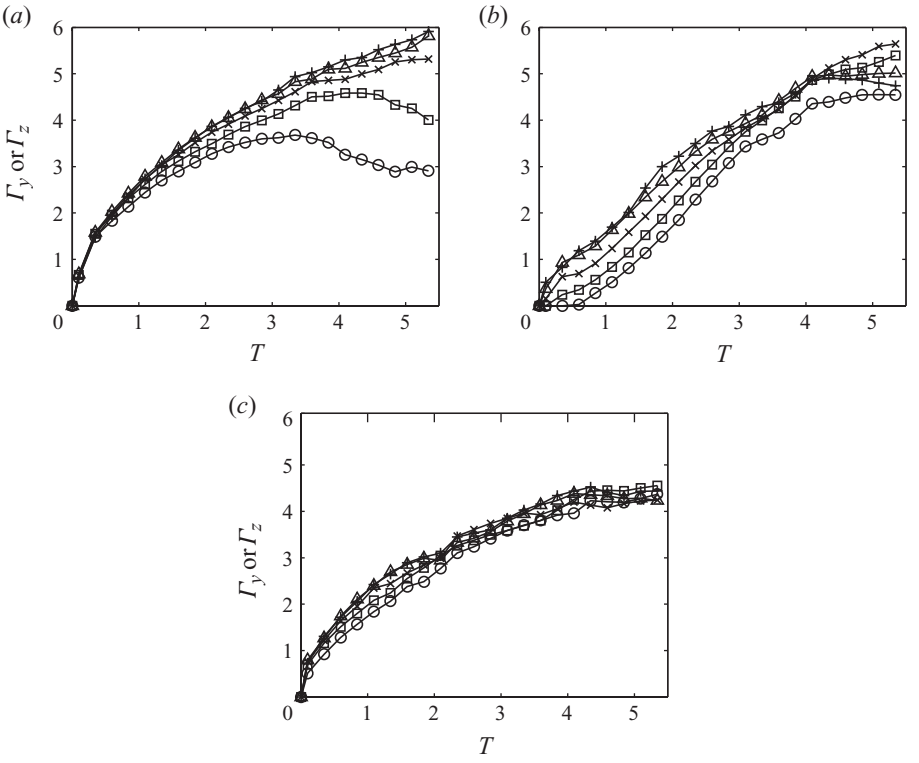

FIGURE 10. Γ_y at the four y-cross sections ($d = 0.38$ (△), $d = 0.50$ (×), $d = 0.62$ (□), $d = 0.74$ (○)) and Γ_z at the $z = 0$ plane (+) for (a) the flat-rigid plate, (b) the flexible plate and (c) the curved-rigid plate. See figure 2(a) for the positions of the sections.

words, the region of high upward flow does not coincide with the LEV cores. For the flexible plate and the curved-rigid plate, the downward flow is prevalent behind the plate rather than the upward flow (figure 9). This downward flow is induced by the LEVs that form along the curved edges of the plates. Because of the downward flow, the interaction of the upward tip flow and the LEVs in the upper region is prohibited. Therefore, early separation of the LEV from the plate does not occur in the upper region. Instead, the upward tip flow blocked by the downward flow is eventually entrained by the LEV in the lower part. Then, the LEV moves away from the plate first in the lower part near the tip (figures 4 and 5). This process results in the formation of a vertical horseshoe-shaped vortex near the lower part of the plate. As mentioned in § 3.1, vortex deformation in the lower region is more apparent in the curved-rigid plate case than in the flexible plate case. The faster development of the LEV in the lower part may induce more distinct vortex deformation in the lower part. Moreover, in the flexible plate case, after the plate deformation is relaxed and the tip bounces back towards its original position, the tip flow starts to move upwards behind the plate (figure 9c). The temporal change of the plate curvature and the resultant change of the upward tip flow distribution cause a less clear vortex deformation in the lower part of the flexible plate, compared to the curved-rigid plate.

3.3. *Vorticity creation and transport*

In order to study vorticity creation and transport by the three translating plates, first, Γ_y at four y-sections and Γ_z at a symmetrical $z = 0$ plane were calculated (figure 10).

Γ_y was defined as $-\int_{A_y} \omega_y \, dA$, where A_y is the total fluid area of a y-section in the positive z side. Only positive z side was considered because of the symmetry condition. In a similar way, Γ_z was defined as $-\int_{A_z} \omega_z \, dA$, where A_z is the total fluid area on the $z=0$ plane. In calculating Γ_y and Γ_z, ω_y and ω_z whose magnitude are smaller than $0.5\,s^{-1}$ were excluded as noise. The size of grids in the experimental data was not fine enough to measure velocity and vorticity fields in the boundary layer region, and the flow field near the base of the plate is absent. Thus, some underestimation of Γ_y and Γ_z may be present in figure 10.

For the flat-rigid plate case (figure 10*a*), Γ_y grows fast when the plate starts impulsively but is followed by a gradual decrease of the slope. While Γ_y in the upper part ($d \leqslant 0.50$) continues to increase, the growth rate of Γ_y in the lower part ($d \geqslant 0.62$) becomes almost zero or even negative. Lack of Γ_y in the lower sections does not mean that ω_y is not created in the lower part of the plate anymore. Instead, vorticity supplied from the boundary layer in the lower sections is lost by convection and tilting processes, which reduce the magnitude of Γ_y in the lower sections. A control volume integral can be used in order to estimate the magnitude of net ω_y transport by tilting and convection on the y-sections. By considering the whole fluid area of a y cross-section in the positive z side as a control volume, we can get the following equation:

$$\frac{d\Gamma_y}{dt} = \int_{A_y} u_y \frac{\partial \omega_y}{\partial y} \, dA - \int_{A_y} \left(\omega_x \frac{\partial u_y}{\partial x} + \omega_z \frac{\partial u_y}{\partial z} \right) dA - \int_{L_y} \nu \frac{\partial \omega_y}{\partial n} \, dL, \qquad (3.1)$$

where A_y is the whole fluid area of the positive z domain at a specified y-section, L_y is the boundary of A_y and the direction of the normal vector n on the boundary is away from the control volume. The term on the left-hand side is the growth rate of Γ_y at the y-section. The first term on the right-hand side means the net growth rate of Γ_y by convection across that y-section. The second term, including the negative sign, is the net growth rate of Γ_y by tilting, and the last term is the ω_y flux from the boundary of A_y by vorticity creation on the plate surface and vorticity cancellation on the symmetrical $z=0$ plane. It is assumed that net diffusion along the y-direction is negligible. ω_y supplied from the boundary can be transported by convection across the y-section and by tilting into the xz-plane, or it can be cancelled on the $z=0$ plane by the merge with the counter-rotating ω_y in the negative z domain.

Figure 11 shows the effect of vorticity transport on the rate of Γ_y in the flat-rigid plate case. Threshold values of vorticity and velocity were applied to obtain the growth rate of Γ_y by convection or tilting at the y-sections; $|\omega_x|$, $|\omega_y|$, $|\omega_z| > 0.5\,s^{-1}$ and $|u_y| > 2\,mm\,s^{-1}$. While net vorticity transport is negligible up to $T=1.5$, Γ_y loss by tilting rather than by convection increases considerably in the lower part of the plate after $T=1.5$. After the tilting rate at $d=0.74$ has the lowest peak at $T=3.8$, the tilting rate at $d=0.62$ has the lowest peaks in turn at $T=4.8$. The LEV tilting occurs from the lower section to the upper section, which is accompanied by the upward motion of the TV. The $d=0.38$ section far from the tip does not have any noticeable net vorticity transport by either convection or tilting during the full observation time. On the other hand, ω_z on the $z=0$ plane is not transported out of the plane, and the net gain or loss of Γ_z by out-of-plane vorticity transport is negligible. The magnitudes of Γ_z on the $z=0$ plane and Γ_y on the uppermost section ($d=0.38$) are similar during the observed time. This similarity is also found in the other two plate cases.

In the flexible plate case, the initial slope of Γ_y is not as large as that of the rigid plate case, especially in the lower part (figure 10*b*). When the plate starts to move, the vortex structure develops faster in the upper part. Therefore, at early formation times,

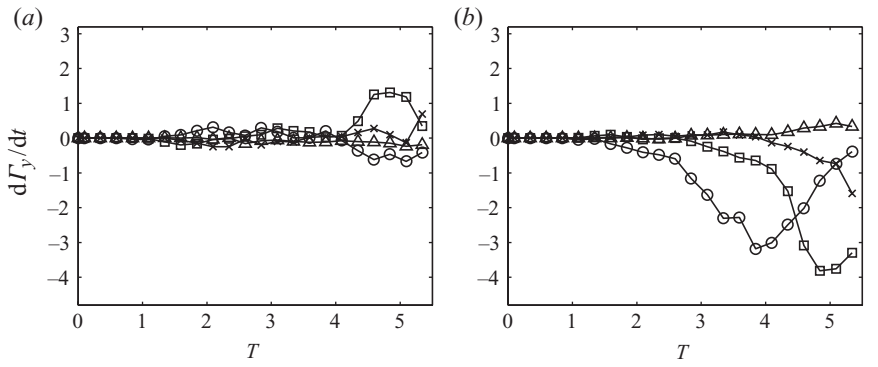

FIGURE 11. Net vorticity transport rates in the flat-rigid plate case ($d = 0.38$ (△), $d = 0.50$ (×), $d = 0.62$ (□) and $d = 0.74$ (○)). (a) is $\dot{\Gamma}_y$ by convection and (b) is $\dot{\Gamma}_y$ by tilting. (a) and (b) are from the first two terms on the right-hand side in (3.1) including the negative sign in front of the term. The negative value in the graphs means Γ_y loss at the section.

Γ_ys of the four y-sections show noticeable variations. Even though the development of the vortex is delayed initially, the vortex grows faster afterwards than that of the flat-rigid plate. From $T = 1.1$ to 3.6, the increments of Γ_y at the four y-sections are larger than that of the $d = 0.38$ section of the flat-rigid plate. During that time span, $\Delta\Gamma_y$ is 3.2 at the $d = 0.74$ section and 2.8 at the $d = 0.38$ section of the flexible plate. Meanwhile, $\Delta\Gamma_y$ is 2.1 at the $d = 0.38$ section of the flat-rigid plate. As a result, near $T = 3.6$, Γ_y of the flexible plate at $d = 0.38$–0.62 becomes as high as that of the flat-rigid plate at $d = 0.62$. The impulsive acceleration of the flat-rigid plate for $T = 0$–0.16 induces the steep growth of the LEV. Meanwhile, the flexible plate accelerates in the x-direction for a longer time (figure 2b). At the four positions of figure 2(b), acceleration continues until $T = 3.6$ even though the forward velocity and acceleration of the plate is not uniform along the span. Therefore, the effect of the acceleration on the increase of the vortex strength extends to $T = 3.6$ even though its effect diminishes gradually as the acceleration magnitude decreases. When the flexible plate bounces back from its maximum deformation after $T = 2.1$, the forward velocity of the plate exceeds the constant velocity of the traverse and reaches the traverse velocity at $T = 5.6$. The larger forward velocity of the plate during this time span is also one of the factors that contributes to the process of vortex creation. For the curved-rigid plate case, the growth rate of Γ_y decreases gradually after initial steep growth, similar to the flat-rigid plate (figure 10c). However, the difference between Γ_y magnitudes for the flat-rigid and curved-rigid plates is more pronounced at the upper part of the plate, $d \leqslant 0.50$. For the $d = 0.38$ section, the difference between Γ_y magnitudes of the two cases is 0.4 at $T = 1.1$ and 0.7 at $T = 4.1$. Moreover, Γ_y does not increase after $T = 4.1$ for the curved-rigid plate. When two counter-rotating LEVs approach each other and the vortex cores are elongated in the curved-rigid plate (figure 5), some cancellation of ω_y of the two LEVs occurs along the $z = 0$ plane. This process results in the loss of Γ_y on the y-sections.

3.4. *Drag force acting on plates*

Figure 12 depicts drag-coefficient measurement by the load cell. In figure 12(a), (2.1a) was used for the definition of drag coefficient C_D. Since the denominator of (2.1a) is the same for the three cases, the magnitude of the measured drags for the three cases can be compared in figure 12(a). In the flat-rigid plate and curved-rigid plate cases,

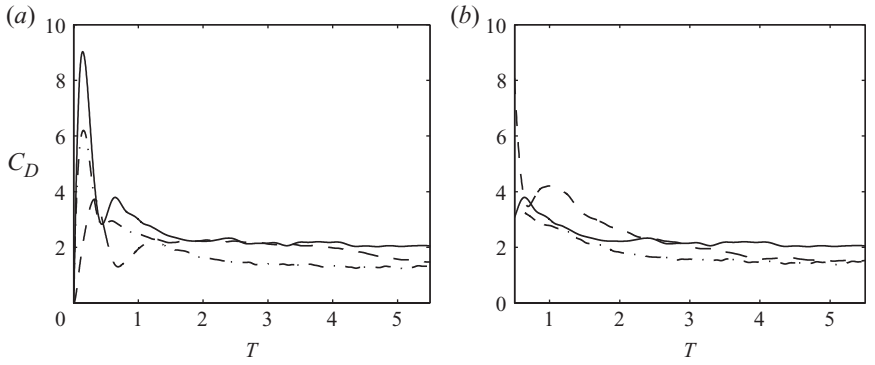

FIGURE 12. Drag coefficients of the translating plates; the flat-rigid plate (—), the flexible plate (– –) and the curved-rigid plate (– · –). The drag coefficients of (*a*) and (*b*) were defined in (2.1*a*) and (2.1*b*). $T = 0$–0.5 is not shown in figure 12(*b*).

the drag has a large initial peak because of sudden acceleration. After the acceleration phase, the drag decreases rapidly from the initial peak and reaches a quasi-steady state. The mean C_D during $T = 0$–2.0 is 3.3 for the flat-rigid plate and 2.7 for the curved-rigid plate. The mean C_D during $T = 2.0$–4.0 is 2.2 for the flat-rigid plate and 1.4 for the curved-rigid plate. A similar trend for the rigid plate was also observed by Dickinson & Götz (1993) and Ringuette *et al.* (2007). The drag of the flexible plate shows a different trend. The magnitude of the initial peak is smaller than those of the two rigid plate cases since the lower part of the plate does not start immediately. However, the drag for the flexible plate reaches large values comparable to that of the flat-rigid plate during $T = 1.5$–4.0. Therefore, the mean C_D (= 2.1) for $T = 2.0$–4.0 is similar to the mean C_D (= 2.0) for $T = 0$–2.0. The C_D of the flexible plate drops after $T = 4.0$ and lies between the drag curves of the other cases. The force trend and magnitude of the flexible plate depend on the flexural stiffness of the plate. Thus, the trend shown in this study should not be applied to plates with different flexural stiffnesses without careful investigation.

In figure 12(*b*), the drag coefficient C_D^* was obtained with (2.1*b*); drag was non-dimensionalised by the instantaneous forward velocity and shape of the plates. Contrary to C_D of figure 12(*a*), C_D^* of the flexible plate decreases from $T = 1.5$ to 4.0. The forward velocity of the plate is larger than the traverse velocity after $T = 2.1$ (figure 2). The increase in the plate's forward velocity beyond the traverse velocity causes the drop in the C_D^* for the flexible plate below the C_D^* of the flat-rigid plate after $T = 2.8$. In this definition of the drag coefficient, the flexible plate has the higher C_D^* than the other cases before $T = 2.8$. The acceleration of the flexible plate is delayed due to its bending deformation. It means the drag increase by acceleration continues until $T = 3.6$, even though its effect diminishes as the acceleration magnitude decreases. Because of prolonged acceleration effect on force generation, the drag per given instantaneous velocity and area (i.e. the second drag coefficient C_D^*) could be larger in the flexible plate case than that of the other cases until $T = 2.8$.

The force acting on a body can be obtained from vorticity field information without the need to know the pressure and shear stress on the body. For a three-dimensional incompressible and viscous flow in an infinite fluid field, which rests at infinity, Wu (1981) derived

$$\boldsymbol{F} = -\frac{\rho}{2}\frac{\mathrm{d}}{\mathrm{d}t}\int_{V_\infty} \boldsymbol{x} \times \boldsymbol{\omega}\,\mathrm{d}V + \rho\frac{\mathrm{d}}{\mathrm{d}t}\int_{V_b} \boldsymbol{u}\,\mathrm{d}V. \tag{3.2}$$

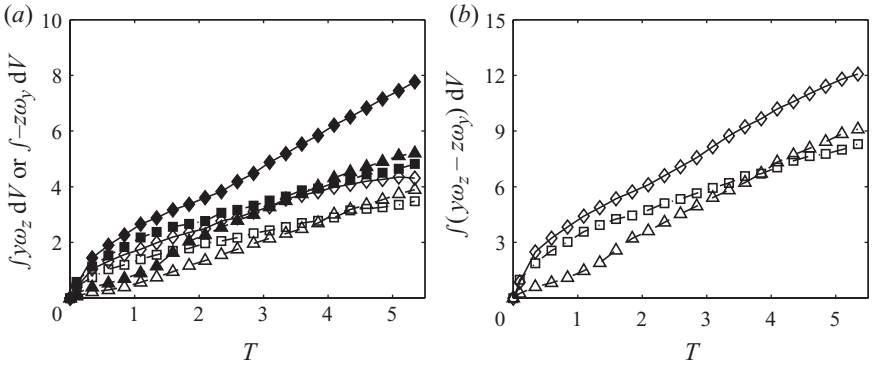

FIGURE 13. Volume integrals of $y\omega_z$ and $-z\omega_y$ over the mapped fluid field. They are non-dimensionalised by $U_c sc^2$. For the three cases, each of $\int y\omega_z \mathrm{d}V$ and $\int -z\omega_y \mathrm{d}V$ is plotted in (*a*). The sum of these two terms, $\int (y\omega_z - z\omega_y)\mathrm{d}V$, is plotted in (*b*). In (*a*), $\int y\omega_z \mathrm{d}V$ (◆) and $\int -z\omega_y \mathrm{d}V$ (◇) for the flat-rigid plate; $\int y\omega_z \mathrm{d}V$ (▲) and $\int -z\omega_y \mathrm{d}V$ (△) for the flexible plate; $\int y\omega_z \mathrm{d}V$ (■) and $\int -z\omega_y \mathrm{d}V$ (□) for the curved-rigid plate. In (b), the flat-rigid plate (◇), the flexible plate (△) and the curved-rigid plate (□).

Then, the drag $D(= -F_x)$ is expressed as

$$D = \frac{\rho}{2}\frac{\mathrm{d}}{\mathrm{d}t}\int_{V_\infty} (y\omega_z - z\omega_y)\,\mathrm{d}V - \rho\frac{\mathrm{d}}{\mathrm{d}t}\int_{V_b} u_x \,\mathrm{d}V, \tag{3.3}$$

where V_b and V_∞ are body volume and total volume including the body, respectively. In order to apply (3.3) to our case, it should first be assumed that the effect of the free surface is negligible and the symmetric flow field can be mirrored across the free surface. The second term on the right-hand side of (3.3) is negligible because the thickness of the plates is small and the traverse driven by the motor moves with a constant velocity after initial acceleration; the magnitude of C_D only by the second term is just 0.24 during acceleration of the flat-rigid plate. According to the first term on the right-hand side in (3.3), newly created vorticity on the surface of the plate can contribute to drag; e.g. negative ω_y created on the positive z-domain of the plate surface increases the first term. In addition, the drag can increase by the transport of vorticity; e.g. negative ω_z moves to the negative y-direction.

Equation (3.3) is useful to investigate how the vortex formation processes of the flexible plate mentioned in the above sections affect the drag trend that is quite different from those of the other two cases (figure 12*a*). The volume integrals of $y\omega_z$ and $-z\omega_y$ ($\int y\omega_z \,\mathrm{d}V$ and $\int -z\omega_y \,\mathrm{d}V$) over the flow field mapped in this study are shown in figure 13. For all three cases, the gap between the magnitudes of $y\omega_z$ and $-z\omega_y$ volume integrals is mainly because the vorticity field near the top of the plate was not included in calculating the volume integral; the top 30 % of the plate was above the mapped flow field. For the flexible plate, the formation of the vortex structure is delayed during early formation time (say, $T < 1.5$) as shown in figures 4 and 10(*b*). Even negative ω_z is distributed only in the upper front surface of the flexible plate instead of the plate tip, which results in smaller $y\omega_z$. These phenomena are closely related to the smaller growth rates of $y\omega_z$ and $-z\omega_y$ volume integrals of the flexible plate than those of the two rigid plates. However, as the flexible plate continues to accelerate beyond the early formation time, the LEV grows rapidly in the lower part of the plate (figure 10*b*). Moreover, the distribution of negative ω_z on the front surface of the plate expands towards the tip (figure 7). Therefore, the

growth rate of $y\omega_z$ and $-z\omega_y$ volume integral sum surpasses that of the curved-rigid plate and becomes comparable to the growth rate of the flat-rigid plate. These vortex dynamics explain why the flexible plate maintains a drag value as high as that of the flat-rigid plate during $T = 1.5$–4.0. The gradual development of vortex size and strength plays an important role in characterising the drag generation of the flexible plate.

4. Concluding remarks

Vortex formation process near the tip region shows distinct difference between the flat-rigid and flexible plates of low aspect ratio. In the flat-rigid plate, the tip flow causes the upward separation of some part of the TV. Simultaneously, it induces the outward motion of the LEV. By early separation of the LEV from the plate, the LEV core in the upper part would be able to maintain the circular shape. In the flexible plate, due to bending of the plate, the upward flow from the tip is suppressed, and the vortex near the tip region forms a horseshoe-shaped vortex. The LEVs of the upper part go through severe elongation along the translating direction of the plate without moving outwards. Previous researchers (Maxworthy 1979; Ellington *et al.* 1996) have reported that the presence of axial flow from the base to the tip on the suction side of the hovering insect's wing stabilises LEV attachment to the wing. In the cases studied here, the axial flow from the tip (upward flow) causes vortex separation and deformation rather than retaining the vortex near the edge of the plate. Furthermore, the distribution of the axial flow is dependent on the plate flexibility. Unlike the wing of hovering insects, our models undergo only a translating motion and the surface of the model is perpendicular to the moving direction. In this respect, the interaction of the LEV and nearby axial flow may depend on the kinematics of the model.

The drag coefficient for the maximally deformed flexible plate is significantly different from that of the curved-rigid plate in a similar shape. This implies that the history of a flow field and plate kinematics should be considered in order to understand the hydrodynamic force generation of a deformable plate. For the flexible plate case, the initial peak of the drag is not as large as the other cases. However, it could maintain the drag comparable to the flat-rigid plate for a long time despite its curved shape. From this study, it was revealed that the slow development of the vortex system by passive deformation of the plate is related to this notable drag trend. An animal with a flexible flapper may be able to avoid the large initial peak of hydrodynamic force at sudden motion and at stroke reversal by slowing down growth of the vortex. This would be beneficial to maintain the constant propulsive force during power strokes, avoid the structural fatigue due to repeated strokes and reduce the excessive demand of muscle work for abrupt stroke conditions. It would be interesting to study how the flexible flapper influences thrust performance and three-dimensional vortex structure around the flapper when it starts to move impulsively.

REFERENCES

Birch, J. M. & Dickinson, M. H. 2001 Spanwise flow and the attachment of the leading-edge vortex on insect wings. *Nature* **412**, 729–733.

Combes, S. A. & Daniel, T. L. 2003*a* Flexural stiffness in insect wings. Part I. Scaling and the influence of wing venation. *J. Exp. Biol.* **206**, 2979–2987.

Combes, S. A. & Daniel, T. L. 2003*b* Flexural stiffness in insect wings. Part II. Spatial distribution and dynamic wing bending. *J. Exp. Biol.* **206**, 2989–2997.

Combes, S. A. & Daniel, T. L. 2003*c* Into thin air: contributions of aerodynamic and inertial-elastic forces to wing bending in the hawkmoth. *Manduca sexta. J. Exp. Biol.* **206**, 2999–3006.

Dickinson, M. H. & Götz, K. G. 1993 Unsteady aerodynamic performance of model wings at low Reynolds-numbers. *J. Exp. Biol.* **174**, 45–64.

Drucker, E. G. & Lauder, G. V. 1999 Locomotor forces on a swimming fish: Three-dimensional vortex wake dynamics quantified using digital particle image velocimetry. *J. Exp. Biol.* **202**, 2393–2412.

Ellington, C. P., Van den Berg, C., Willmott, A. P. & Thomas, A. L. R. 1996 Leading-edge vortices in insect flight. *Nature* **384**, 626–630.

Gharib, M., Rambod, E. & Shariff, K. 1998 A universal time scale for vortex ring formation. *J. Fluid Mech.* **360**, 121–140.

Koumoutsakos, P. & Shiels, D. 1996 Simulations of the viscous flow normal to an impulsively started and uniformly accelerated flat plate. *J. Fluid Mech.* **328**, 177–227.

Maxworthy, T. 1979 Experiments on the Weis-Fogh mechanism of lift generation by insects in hovering flight. Part 1. Dynamics of the fling. *J. Fluid Mech.* **93**, 47–63.

Mountcastle, A. M. & Daniel, T. L. 2009 Aerodynamic and functional consequences of wing compliance. *Exp. Fluids* **46**, 873–882.

Pereira, F. & Gharib, M. 2002 Defocusing digital particle image velocimetry and the three-dimensional characterization of two-phase flows. *Meas. Sci. Technol.* **13**, 683–694.

Pereira, F., Stuer, H., Graff, E. C. & Gharib, M. 2006 Two-frame 3D particle tracking. *Meas. Sci. Technol.* **17**, 1680–1692.

Pullin, D. I. & Wang, Z. J. 2004 Unsteady forces on an accelerating plate and application to hovering insect flight. *J. Fluid Mech.* **509**, 1–21.

Ringuette, M. J., Milano, M. & Gharib, M. 2007 Role of the tip vortex in the force generation of low-aspect-ratio normal flat plates. *J. Fluid Mech.* **581**, 453–468.

Spedding, G. R., Rosen, M. & Hedenstrom, A. 2003 A family of vortex wakes generated by a thrush nightingale in free flight in a wind tunnel over its entire natural range of flight speeds. *J. Exp. Biol.* **206**, 2313–2344.

Srygley, R. B. & Thomas, A. L. R. 2002 Unconventional lift-generating mechanisms in free-flying butterflies. *Nature* **420**, 660–664.

Vogel, S. 1996 *Life in Moving Fluids*. Princeton University Press.

Wang, Z. J. 2004 The role of drag in insect hovering. *J. Exp. Biol.* **207**, 4147–4155.

Willert, C. E. & Gharib, M. 1992 Three-dimensional particle imaging with a single camera. *Exp. Fluids* **12**, 353–358.

Wu, J. C. 1981 Theory for aerodynamic force and moment in viscous flows. *AIAA J.* **19**, 432–441.

Young, J., Walker, S. M., Bomphrey, R. J., Taylor, G. K. & Thomas, A. L. R. 2009 Details of insect wing design and deformation enhance aerodynamic function and flight efficiency. *Science* **325**, 1549–1552.